We are IntechOpen, the world's leading publisher of Open Access books Built by scientists, for scientists

4,800
Open access books available

122,000
International authors and editors

135M
Downloads

Our authors are among the

154
Countries delivered to

TOP 1%
most cited scientists

12.2%
Contributors from top 500 universities

WEB OF SCIENCE™

Selection of our books indexed in the Book Citation Index in Web of Science™ Core Collection (BKCI)

Interested in publishing with us?
Contact book.department@intechopen.com

Numbers displayed above are based on latest data collected.
For more information visit www.intechopen.com

19

Volumetric Monitoring and Modeling of Indoor Air and Pollutant Dispersion by the Use of 3D Particle Tracking Velocimetry

Pascal Biwole[1], Wei Yan[2], Eric Favier[3],
Yuanhui Zhang[2] and Jean-Jacques Roux[3]
[1]*University of Nice Sophia Antipolis,*
[2]*University of Illinois at Urbana-Champaign,*
[3]*University of Lyon,*
[1,3]*France*
[2]*USA*

1. Introduction

Human beings spend most of their lifetime indoors. Monitoring indoor airflow in buildings is a matter of health safety, and energy savings. Regarding health safety it is proven that exposure to aerosol pollution like walls and painting material residues, gasses emitted through cooking and heating with biomass fuel, or agricultural residues can result in aggravated health damages for the occupants. In the same time, too high air exchange rates increase the heating demand in temperate and cold climates. On both cases it is important to control the mixing of the air and the pollutant dispersion to ensure the occupants' comfort and productivity.

Before monitoring air mixing and pollutants dispersion in rooms, one has to decide whether qualitative or quantitative data is needed. Qualitative measurements only allow recovering the trajectory and patterns of the airflow in rooms. This is usually done by the use of tracer gasses like fumes, incense, or neutrally buoyant particles with suitable light sources. For more precise purposes such as comfort parameters measurements (Fanger, 1970) or validation of CFD modeling, one need to get access to quantitative data.

Quantitative air measurement techniques may be divided into Eulerian and Lagrangian techniques. Eulerian techniques measure flow velocity at one or several fixed locations at a time, as a man on a bridge measures the velocity of a water stream going by below him. Eulerian methods used for indoor applications include hot wire and hot film anemometry, pulsed wire anemometry, ion anemometry, laser Doppler velocimetry, laser 2-focus velocimetry, particle image velocimetry (PIV), stereoscopic PIV, tomographic PIV and holographic PIV. Depending on the technique, the result can be a one, two, or three-dimension velocity vector or velocity vector field.

But Eulerian techniques suffer from two major drawbacks: First, many are intrusive since they involve probes which are inserted in the measured flow. The probes not only change the flow by their mere presence, but they also disturb the measure. For example, though hot

wire anemometers are widely used in indoor air research, they can produce a 50% error on low ascendant flows because the hot probe creates its own convection, which becomes predominant. Moreover, most hot wire anemometers cannot achieve quantitative measurements of indoor air speeds lower than 10cm/s. Hot-films can reach 2cm/s, but the velocity orientation then becomes unavailable. Second, most Eulerian techniques only yield point-wise velocity measurements and are therefore ill-adapted to indoor air flows because they are unsteady and highly three dimensional. For example, Laser Doppler velocimetry can only yield the 3D velocity field inside a measuring volume of a few millimetres large. This method is generally restricted to near-the-wall boundary layers measurements. Stereo-particle image velocimetry can recover the instantaneous 3D velocity of large fields, but only for particles situated inside 3 to 10mm-large laser sheets.

To cope with those impediments, scientists have tried to build Lagrangian measurement techniques for nearly three decades: instead of measuring fluid properties from a fixed measurement point, the goal is to actually ride the flow as on a boat, thanks to neutrally buoyant particles, and monitor the flow's fluctuations. The more particles we have in the fluid, the finer our understanding of its topology. Each individual seeded particle is followed through time, in order to get its trajectory. Consequently, Lagrangian techniques provide a better spatial resolution than Eulerian techniques. There are two main Lagrangian methods under development for indoor air applications:

1.1 Particle streak velocimetry

Particle streak velocimetry (PSV) uses neutrally buoyant particles whose displacement is seen as streaks by setting a long camera exposure time (Dimotakis et al., 1981). Trajectories are yielded when the dead time between two long exposures is very short, depending on the flow velocity. Each streak's pixel length and orientation can be calculated as the length and orientation of the major axis of the ellipse that has the same normalized second central moments as the streak region. Dividing the streak length by the exposure time gives the velocity. The third velocity component can be acquired by geometric reconstruction in a stereoscopic system of at least two cameras (see Figure 1). The particle streak direction can be obtained by setting one of the three cameras with a shorter exposure time (Scholzen & Moser, 1996).

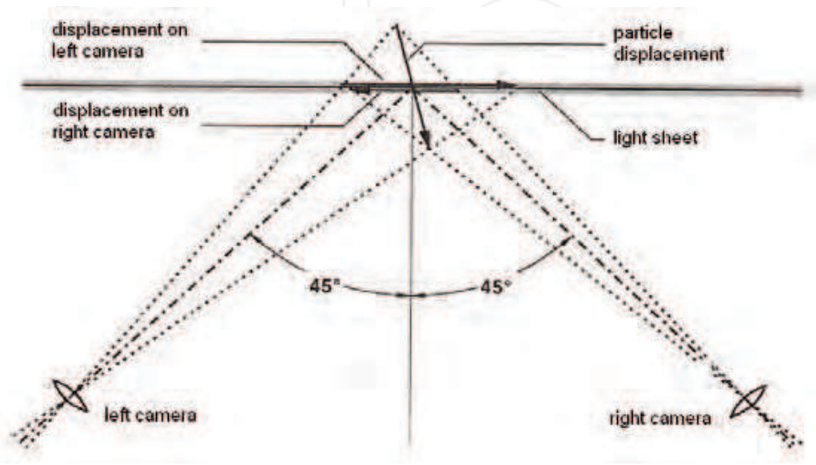

Fig. 1. Geometric reconstruction of the third displacement component in a stereoscopic system

Even though PSV has yielded promising results in indoor applications (Machacek, 2002; Sun & Zhang, 2003) the technique suffers from three structural limitations: Firstly, the flow velocity has to be high enough for particles to create streaks on camera image planes. This is not always possible with indoor air flow as a target. Secondly, many particle streaks may be bowed, especially where turbulence takes place. Additional approximation to reconstruct the streak length is then unavoidable. Thirdly, the velocity is always calculated as a mean over the length of the streak, thus somewhat limiting the spatial resolution of the method.

1.2 Particle tracking velocimetry

In particle tracking velocimetry (PTV), particles are detected as single points on each image by setting a very short camera exposure time. Velocity is calculated by dividing the displacement on object planes by the time between two exposures. PTV yields 3D trajectories by using at least two cameras. Depending on the algorithms used, either particles are first identified (spatial matching) then individually tracked (temporal tracking), or inversely 2D trajectories are first searched separately on each camera before being matched. A few schemes to achieve temporal tracking and spatial matching will be detailed later in this chapter.

The main drawback of 3D PTV is the difficulty of finding and tracking particles which overlap when the seeding density is strong. Therefore, densities need to be maintained low, typically about 0.005 particles per pixel for a system with three cameras (Maas et al., 1993). Other drawbacks of PTV are the limited number of suitable tracers and the fact that precisely measured 3D positions cannot be prescribed in advance. In spite of those drawbacks, PTV features a better spatial and temporal resolution than PSV. Calculated 3D velocities range from 0m/s to a maximum speed depending on the speed of the recording camera and on the intensity of the light source. Modern cameras go over tens of KHz but a very powerful light source is then needed to capture particle images.

The literature shows that over the past 15 years, most research on 3D PTV has been dedicated to volumes from Kolmogorov scales (Virant and Dracos 1997, Lee and Kim 2005) to centimetric scales (Suzuki et al., 2000). Small scale 3D PTV can track more than 1000 to 1500 particles. 3D PTV in air volumes over 1 m^3 has seldom been done. It raises new challenges in terms of illumination and camera positioning, but also in terms of particle size and localization. Pulsed lasers used in small-scale PTV (Adrian, 1991; Ouellette et al., 2006; Willneff and Gruen, 2002) cannot be used on larger volumes because the energy density of the light decreases rapidly when the beam is expanded. Nanometric and micronic particles used in small-scale PTV are extremely difficult to track in big volumes with a reasonable density. The use of at least three cameras positioned at large angles with respect to the other cameras is crucial to reducing measurement errors. In contrast to small-scale PTV, particle size and brilliance vary a lot since they are free of movement. In fact, particles close to the cameras create large blobs on the images.

The purpose of this chapter is to present the 3D particle tracking velocimetry (3D PTV) method applied to the monitoring of air displacements and pollutant dispersion in rooms. 3D PTV is searched in order to yield the three dimensional velocity and the trajectory of the air in a single zone versus time. Air exchange measurement and air leakage measurement are not within the scope of this chapter. Similarly, the measurement of airflow through ducts, fans and heat exchangers will not be covered herein, even though the 3D PTV may be extended to that use.

The layout of the chapter will be as follows: Section two will present the experimental set up required to perform 3D PTV in rooms. Special attention will be given to the choice of the tracer particles. Section three will briefly explain the layout of the most common 3D PTV algorithms. In particular, an image processing procedure to remove speckles from images of particles getting close to the cameras will be detailed. Section 4 will show a few examples of the results one might get when using the method. Some helpful guidelines will be provided in terms of camera and light positioning, depending on the room layout and wall color. Last, Section 5 will clearly state the limitations of the method, and present a few trends about the ongoing research on the subject.

2. 3D PTV experimental set-up

2.1 Choice of the tracer

The three major parameters for choosing a fluid tracer in any particle image velocimetry method are a neutral density with respect to the fluid, a detectability of the particles by the cameras, and a size and lifetime that suits the scale and duration of the flow characteristics to be measured. Other minor requirements are a low environmental impact (health hazards, corrosion on equipment, waste disposal) and an easy storage and manipulation. An extensive list of possible tracers for PIV tests was given by (Melling, 1997). For gaseous flows he proposes particles from olive oil, wheat oil, oil fumes, glass, polycrystalline, AL_2O_3, TiO_2, and ZrO_2. (Adamcyzyk & Rimai, 1988) also used nylon micro-balloons for 3D PTV in the air in a 5 x 5 x 5 cm section. All those tracers range from less than 1µm to 30 µm. For detecability purpose, they are always used with pulsed laser light. In spite of their good size for turbulence patterns visualization, the use of such minute particles is impossible in volumes as large as ours because they cannot be singled out and tracked.

In large scale air volumes with feeble pressure gradient, most researchers use helium filled soap bubble (Biwole et al. 2009; Kessler & Leith, 1991; Machacek, 2002; Müller & Renz, 1996; Okuno et al., 1993; Sholzen & Moser, 1996; Sun and Zhang, 2003; Suzuki & Kazagi, 1999; Zhao et al., 1999). The underlying idea is that a liquid film inflated with a lighter-than-air gas can produce a neutrally buoyant particle. Those particles fulfill most requirements mentioned above, except when studying small scale turbulence patterns because of their size (from 1.3mm to 3.8mm, Anonymous, 1988).

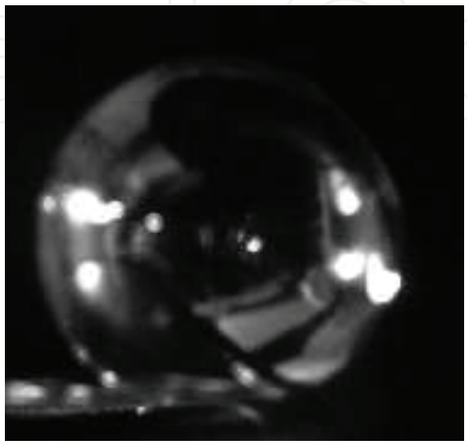

Fig. 2. Bright spot on a single helium filled soap bubble (from Machacek 2002)

The motion of a bubble can be derived from the equation of the movement of a small rigid sphere in a non-uniform and incompressible flow (Maxey & Riley, 1983):

$$m_p \frac{dv_p}{dt} = (m_p - m_f) g_v + m_f \left. \frac{Dv_f}{Dt} \right|_{Y(t)} - \frac{1}{2} m_f \frac{d}{dt} \left\{ v_p(t) - v_f\left[Y(t), t\right] - \frac{1}{10} a^2 \nabla^2 v_f \Big|_{Y(t)} \right\} - \tag{1}$$

$$6\pi a \mu \left\{ v_p(t) - v_f\left[Y(t), t\right] - \frac{1}{6} a^2 \nabla^2 v_f \Big|_{Y(t)} \right\} - 6\pi a^2 \mu \int_t^\tau \left(\frac{d / dt' \left\{ v_p(t') - v_f\left[Y(t'), t'\right] - \frac{1}{6} a^2 \nabla^2 v_f \Big|_{Y(t')} \right\}}{\left[\pi \nu (t - t')\right]^{1/2}} \right) dt'$$

with m_p being the bubble mass, m_f the mass of fluid displaced by the sphere, v_p the speed of the buble, g_v the acceleration due to gravity, v_f the speed of the fluid, $Y(T)$ the center of the sphere at time t, a the radius of the sphere, μ and ν respectively the dynamic and kinematic viscosities of the fluid. If we make the assumptions that the flow is irrotational, that the bubbles remain spherical throughout their lifetime and that interactions among bubbles are negligible, Maxey and Riley equation simplifies into (Kerho & Bragg, 1994):

$$\begin{aligned} m_p \frac{dv_p}{dt} &= (m_p - m_f) g + m_f \frac{Dv_f}{Dt} - \frac{1}{2} m_f \left(\frac{dv_p}{dt} - \frac{Dv_f}{Dt} \right) \\ &+ \frac{1}{2} \rho C_D S \left| v_f - v_p \right| \left(v_f - v_p \right) + 9 m_p \sqrt{\frac{\mu \rho}{\pi D^2 \sigma^2}} \int_0^t \frac{d / dt' \left(v_f - v_p \right)}{\sqrt{t - t'}} dt' \end{aligned} \tag{2}$$

where D represents the diameter of a bubble, ρ the density of the air, σ the density of the bubble, C_D the coefficient of drag of the bubble, and S the apparent surface (half sphere surface). The left hand term of equation 1 represents the inertia force while the right hand terms are respectively the buoyancy force, the pressure force, the added mass, the drag term and the Basset force. If we assume that the slip velocity and the slip acceleration both present in the right-hand term of Eq. 2 are negligible, the equation becomes:

$$m_p \frac{dv_p}{dt} = (m_p - m_f) g + m_f \frac{Dv_f}{Dt} \tag{3}$$

The meaning of Eq. 3 is that the movement of a small particle in a flow depends primarily on the forces of pressure, inertia and gravitation. For a particle with neutral density with respect to the fluid, $m_p = m_f$. In that case, pressure forces are balanced by inertia forces. For a particle lighter than the fluid, we have $m_p < m_F$. The bubble will tend to deviate and to be elevated from the real streamlines. The constant diameter assumption is plausible given the weak air temperature and pressure gradients usually observed indoors. But when using helium filled bubbles as tracers for 3D PTV indoor, the experimenter have to keep in mind that the slip velocity and the slip acceleration between the bubble and the surrounding air may not be zero. This is a major assumption and still an open question.

2.2 Choice of the cameras

Three main features have to be taken into account when choosing a camera for flow visualization:

- The maximum frame rate: The frame rate is primarily chosen relatively to the maximum flow velocity. The quicker the flow, the higher the frame rate must be. In traditional PIV, the maximum time between two frames is calculated so that the fluid displacement is less than a quarter of the size of research windows. 3D PTV globally follows the same rule. The frame rate has also to be adjusted to the particle seeding density in order to help minimizing tracking ambiguities. The denser the seeding, the quicker the camera must be. For indoor air speeds, 100fps cameras generally allow a satisfying tracking of the flow.
- The camera resolution: It is chosen depending on the size of the particles employed, the size of the field to be visualized - the larger the field, the higher the resolution must be -, the illumination employed, and the background. In a case of poor contrast with the background or when the light sheet is very large, sensors featuring a high number of gray levels should be preferred, typically with at least 8 bits i.e. 2^8 of gray levels. Large pixel size cameras provide better sensitivity but poorer resolution than cameras with smaller pixel size. Color images are not preferred in PTV because the complexity of the algorithms is increased for a limited gain. Whatever the number of cameras, they must all be time-synchronous.
- The lenses: Fish-eyed lenses may be chosen (Biwole et al. 2008; Biwole et al. 2009) for indoor applications, provided the calibration procedure is powerful enough to calculate the distortion coefficients and reconstruct the scene.

2.3 Choice of the light source

The light source has to be strong and homogeneous enough for the cameras to see the light reflected on the tracer shells in every part of the measurement field. Especially in 3D PTV in large volumes, this must be true even for particles situated outside of the cameras object plane. Besides, the wavelength reemitted has to fit the spectral sensitivity of the recording sensor. Finally, light devices must produce low convective heat in order to keep the flow undisturbed. The light sources can be either pulsed or continuous. Pulsed lasers used in small scale PTV cannot be used on larger volumes because the energy density of the light decreases rapidly when the beam is expanded. For indoors applications, continuous type illumination solutions are usually preferred because it avoids synchronizing the light with the cameras. Arc lamps equipped with a cylindrical lens (Sholzen & Moser, 1996) or especially powerful halogen spot lamps (Machacek, 2002; Sun & Zhang, 2003; Biwole et al., 2009) are generally used. To reduce heat generation, the light sources can either be placed outside of the test room behind a glass panel, or switched on for only the few seconds of the recording.

To conclude on this section, tests *in situ* in presence of the particles, the cameras and the light sources are always necessary before settling for any specific equipment.

3. 3D PTV algorithms

3.1 Calibration

Before recording the seeded air, all the cameras must be calibrated. Calibration is the process of calculating the parameters taking part in the mathematical relationship between the 2D image coordinate system of each camera and a 3D real world coordinate system common to all cameras. Those parameters are actually the output of the calibration process.

Firstly, the coefficients yielded by camera calibration are the intrinsic parameters of each camera, i.e. the focal length, the radial and tangential distortion coefficients, the principal point

pixel coordinates and the skew coefficient defined as the angle between x and y pixel axes on the CCD (Charge-Coupled Devices) or CMOS (Complimentary Metal-Oxide Semiconductor) chip. Secondly calibration yields the extrinsic parameters of each camera, namely the rotation and translation matrices mapping each camera 3D coordinate system based at the center of the lens, to the common 3D coordinate system defined by the calibration target (see Figure 3). Thus, if Ti and Ri are respectively the 3 × 1 translation matrix and the 3 × 3 rotation matrix which transform camera i 3D reference frame XXci into the calibration target 3D reference frame XX, the relationship between the two coordinate systems reads:

$$XXci = Ri \cdot XX + Ti \tag{4}$$

Intrinsic and extrinsic parameters are calculated by minimizing the distance between actual specific points on a calibration target or a scene, and their simulated location based on the fitting of a mathematical camera model.

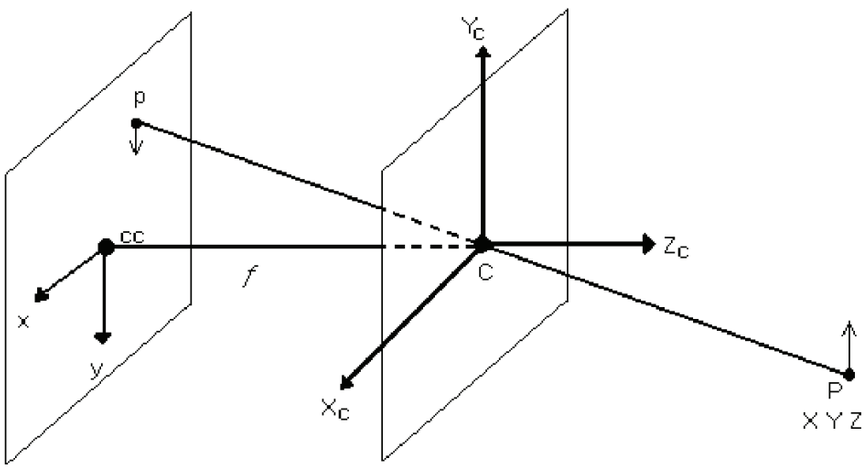

Fig. 3. Image plane coordinate system (cc,x,y) and camera coordinate system (C,Xc,Yc,Zc) in the pinhole camera model. Coordinates of point P(X,Y,Z) are given in a real world 3D coordinate system which origin is the origin of the calibration target.

There are roughly two different camera calibration methods (Zhang, 1999): Photogrammetric calibration and self-calibration. In photogrammetric calibration, a 3D object with precisely known features is observed. The calibration object generally consists of two or three perpendicular planes with square or round black and white patterns. Photogrammetric calibration can be done very accurately (Faugeras, 1993) but requires a very precise and expensive calibration set-up. Self-calibration doesn't require any calibration object. The calibration parameters are derived (Hartley 1994, Luong and Faugeras, 1997; Maybank & Faugeras, 1992) by observing a static scene from a moving camera. Yet flexible, this method is not yet mature (Bougnoux, 1998) and results obtained are not always reliable. Other calibration methods exist, including the vanishing points for orthogonal directions method (Caprile & Torre, 1990; Liebowitz & Zisserman, 1998) and the pure rotation calibration (Hartley 1994, Stein 1995).

The multi-camera calibration is done by recomputing the extrinsic parameters of all cameras from a single position of the calibration target simultaneously viewed by all the cameras (see Figure 4). After calibration, the cameras must not be moved during the whole recording

session. This would cause a change in the value of the extrinsic parameters. Though camera calibration is usually performed prior to image acquisition, it can also be done after recording the particle images, provided the cameras have not been moved.

Fig. 4. The calibration target must be viewed simultaneously by all cameras when computing the common real world reference frame

3.2 Particle detection

The aim of the particle detection procedure is to compute the pixel coordinates of each particle center. Unlike traditional 3D PTV, PTV algorithms for large indoor air volumes must include a step where oversized particles images are removed from the images. Those oversized particle images are here referred to as "blobs". They are created by images of helium filled bubbles getting close to the cameras, since they are not constrained to remain inside a small delimited volume. Bubbles creating those blobs are generally out of the common field of vision. The particle detection processes usually includes the following steps:

1. Creation and subtraction of background from images.
2. Blob removal.
3. Calculation of pixel coordinates.

3.2.1 Creation and subtraction of background from images

The purpose of this step is to feed the tracking algorithm with grey level images of particles over totally black background images. The creation of the background is generally made by averaging a certain amount of images. Averaging the background is used to cope with the variations of continuous light intensity. It can be made in the presence of particles but conducting this process before introducing particles (or after all particles are gone) gives better subtraction results. When averaging the background in the presence of particles, it is worth averaging the whole set of particle images to be treated by the tracking algorithm. When averaging without particles, one should not use more than about 10 images otherwise the resulting image gradually becomes saturated.

After being created, the background is subtracted from each image. However, the result of the process generally does not permit a clear separation of particle images from residual noise. The main image processing functions usually used to remove noise are:

- Thresholding: This operation consists in retaining only the pixels which luminance is above a certain value determined empirically. Since noise has generally a luminance lower than particles, thresholding permits getting good images of particles. Finding the appropriate threshold can be made experimentally (the operation is rather quick) but it can also be implemented automatically, for instance by minimizing the interclass-variance of the segmented black and white pixels (Otsu, 1979).
- Removal of isolated pixels: Helium filled soap bubbles generally cover more than one pixel. Typically they create speckles of diameter three to six pixels. Therefore, isolated pixels can more than often be assimilated to remaining noise. They can be removed by eroding the image with structuring elements of 2-pixel lengths.

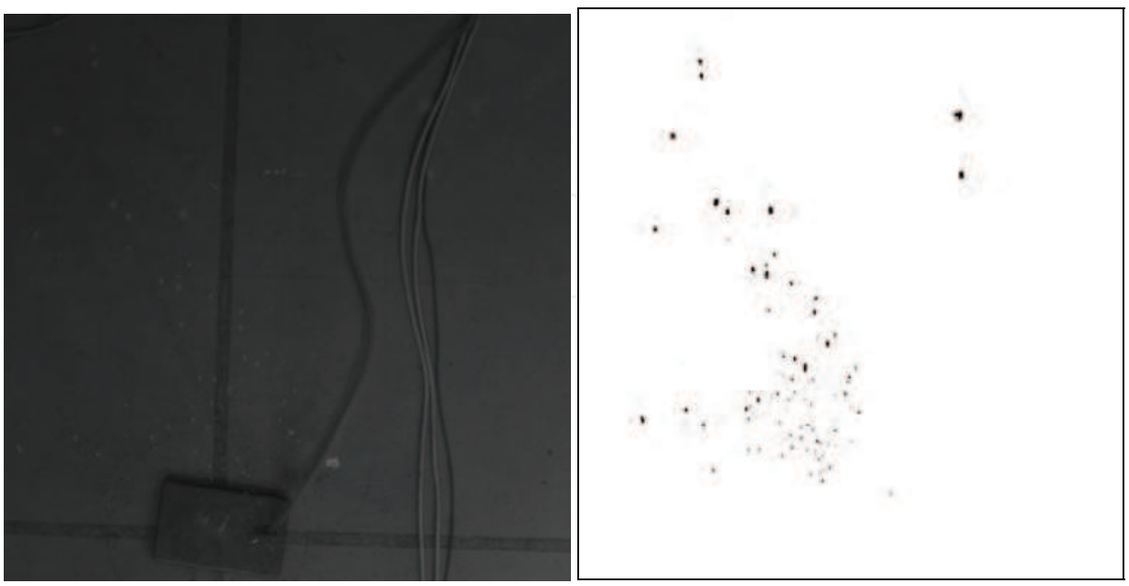

Fig. 5. Particle image before and after background and noise removal (the processed image is inverted for better clarity)

3.2.2 Blob removal

Blobs must be removed from the images because every single blob displays many isolated pixels, thus leading to false particle detection (see Figure 6). Removing round objects of a certain diameter from an image is a standard procedure in image processing called opening. An opening is an erosion followed by a dilation using the same structuring element for both operations. However, this operation generally gives poor results with images of helium filled bubbles. Since the particle images are neither perfectly round nor perfectly filled, the bubble shells can generally be seen after the processing, as shown in Figure 7. After removing the averaged background, blobs can be efficiently removed by the following procedure:

1. Binarize the image. The binary threshold level can be assigned empirically, or automatically calculated from iterative algorithms (Crouser et al. 1997; Otsu, 1979).
2. Fill-up and bridge all particle images in order to get homogeneous blobs (see Figure 8a). This filling-up and bridging may be made by iteratively dilating the image with structuring elements [1,1] and [1,1]T.
3. Erode the output image with a square structuring element of size the maximum diameter of a particle in the common camera's field of vision (see Figure 8b). Here particles of diameter equal or less than the maximum allowed are removed from the image. This maximum diameter value is determined empirically.
4. Dilate the resulting image with a square structuring element larger than the one previously used. Good results were achieved with a structuring element twice the size of the first one used (see Figure 8c).
5. Subtract the output image from the original unbinarized particle image (image before applying the first step of the procedure) to keep the Gaussian profile of the bubble images. The resulting image only contains particles of diameter equal or less than the size of the structuring element in step 3 (see Figure 9).

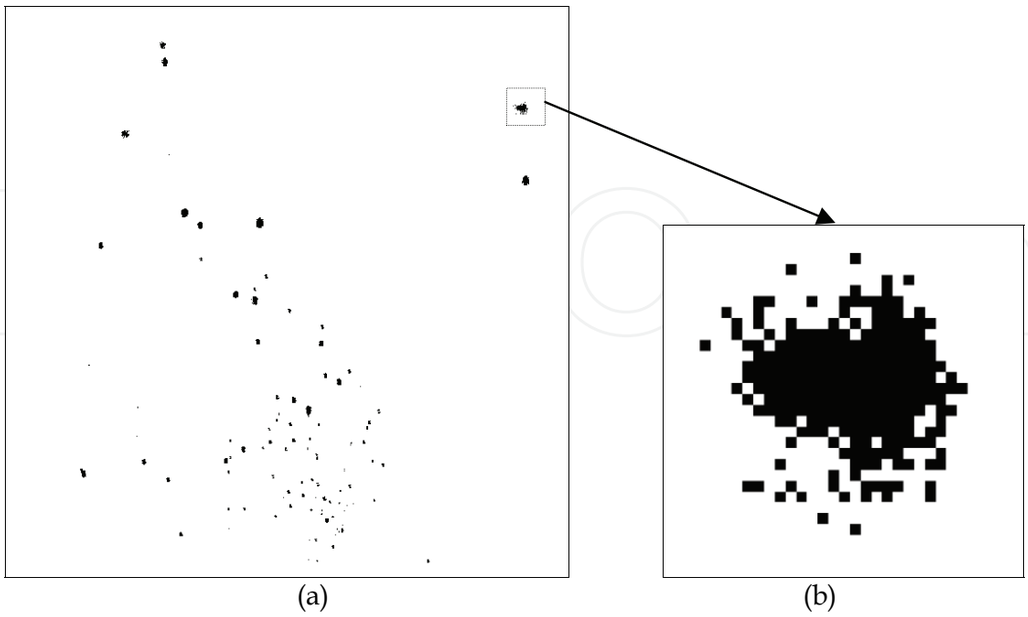

(a) (b)

Fig. 6. (a) Binarized particle image before blob removal (the image is inverted for clarity). (b) Standard over-large particle (blob). Blobs create many centroids leading to false detections

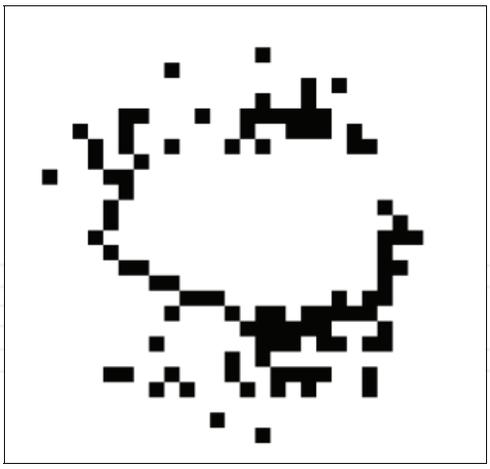

Fig. 7. Over-large particle image after standard image opening with an 8-pixel large disk-shaped structuring element. Bubble's shell is still visible

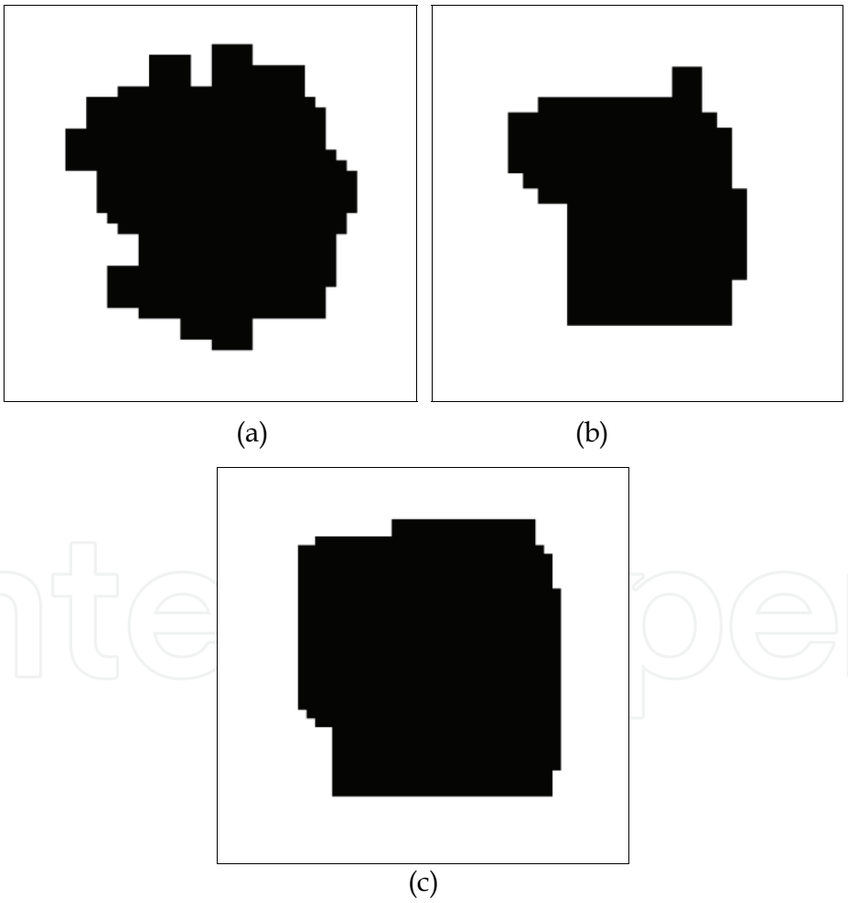

Fig. 8. Proposed procedure for blob removal: (a) Blob filled and bridged. The displayed blob covers a 28x27 pixel region. (b) Same blob after an erosion with an 8-pixel square-shaped structuring element (16x15 pixel region). (c) Same blob after dilatation with a 16-pixel square-shaped structuring element (31x30 pixel region)

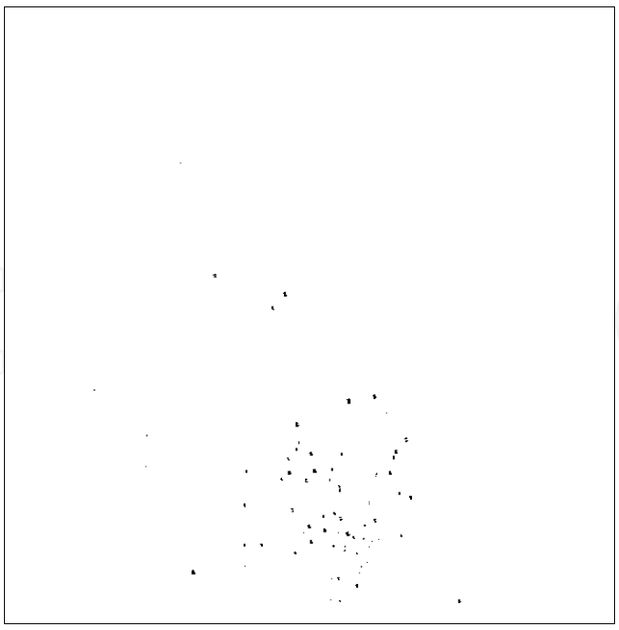

Fig. 9. Example of output image after the blob removal procedure. The image only contains particles of diameter less than 9 pixels

3.2.3 Calculation of particle centers pixel coordinates

Particle centers pixel coordinates are here referred to as "centroids". When calculating centroids from helium filled bubble images, template matching (Gruen & Baltsavias, 1988; Guezennec et al., 1994) gives poor results with soap bubbles because of the wide range of particle shapes and sizes after image processing. Hough transform (Hough, 1962) is ill-adapted to the smallness of the pixel area covered by average particles which varies from 2x2 to 8x8 pixels, depending on the distance from the cameras. Invariant second order grey moments method (Teh & Chin, 1988) works well when only two particle images are overlapping but fail when three particles create a larger speckle. Higher order moments are very noise sensitive. 2D Gaussian fitting (Mann et al., 1999; Nobach & Honkanen 2005) works well when particles intensity profile can be approximated by a Gaussian. In our case, a single particle often features two intensity peaks. In addition, Gaussian fitting is computationally costly and gives better results on large particle images. The same drawbacks work for neural network methods (Carosone et al., 1995) though those methods are robust in case of noisy images.

As shown in Figure 2, particles are seen as two (or only one) bright spots on the particle shell symmetric relative to the center of the sphere. This fact makes relevant the use of weight averaged methods to calculate the center of mass of each particle. For each particle, the coordinates (x_c,y_c) of the center or mass are given by:

$$x_c = \frac{\sum xI(x,y)}{\sum I(x,y)} \;;\; y_c = \frac{\sum yI(x,y)}{\sum I(x,y)} \tag{5}$$

where *(x,y)* are the pixel coordinates of each pixel belonging to the particle and *I(x,y)* the pixel luminance. This method allows recognizing two connected bright spots as a single

particle. Its main shortcoming is the creation of two centroids whenever the two bright spots are not connected (see Figure 10).

Fig. 10. Output of the center of mass calculation by weight averaging on three particles of the same image. Far left and center particles yield one centroid whereas far right particle displays two disconnected local maximum and therefore yields two centroids

As shown by (Ouellette et al., 2006), weight averaging methods may be less accurate than Gaussian fitting and neural network methods whenever particles are far enough from the camera to feature a single local maximum. Nevertheless, this method is efficient, readily implemented and rapid. Particle centers are given with sub-pixel accuracy (down to 1e-01) with derisive computation time using standard personal computers. Furthermore, in large volumes (over $1m^3$), overlapping cases are estimated to less than 5% of particle images for camera resolutions over 1024x1024 pixels.
Once we can accurately detect particle centers on each image, the next step is to establish their 2D or 3D trajectory from successive images. That is particle tracking.

3.3 Particle tracking

Particle tracking schemes used for 3D PTV in large scale indoor air applications do not differ from particle tracking schemes used in other applications. Particle tracking schemes can be divided into three main categories:

- Image plane based tracking schemes: Particles are tracked on each camera 2D image plane separately through time (temporal tracking). Afterwards, the resulting 2D trajectories are matched in 3D object space and the 3D coordinates are calculated (Biwole et al., 2009; Engelmann, 1998, 2000; Ge & Cha, 2000; Guenzennec et al., 1994; Jähne, 1997; Li et al. 2008; Wierzimok & Hering, 1993)
- Object plan based tracking schemes: Particle 3D coordinates are first calculated at each time step separately. Afterwards, the resulting set of time-ordered 3D coordinates is the only input for temporal tracking directly in object space. The correspondence problem is addressed at the first or only a few time steps of the image sequence (Kasagi & Sata, 1992; Maas, 1992; Maas et al., 1993; Malik et al., 1993; Nishino et al., 1989; Nishino & Kasagi, 1989; Papantonious & Dracos, 1989; Sata et al., 1994; Suzuki et al., 2000; Virant, 1996; Willneff & Gruen, 2002)

In spite of their high potential the object plan based tracking algorithms hold two main drawbacks: first, the repetitive error in the calculation of particle 3D coordinates aggregates as the trajectory gets longer. Second, the unsolved particle 3D correspondences create many discarded particles and broken trajectories. On both schemes, Particle tracking from one time frame to another is usually based on a set of criteria such as the minimum change in particle acceleration, the particle shape and the particle luminance. An additional cost

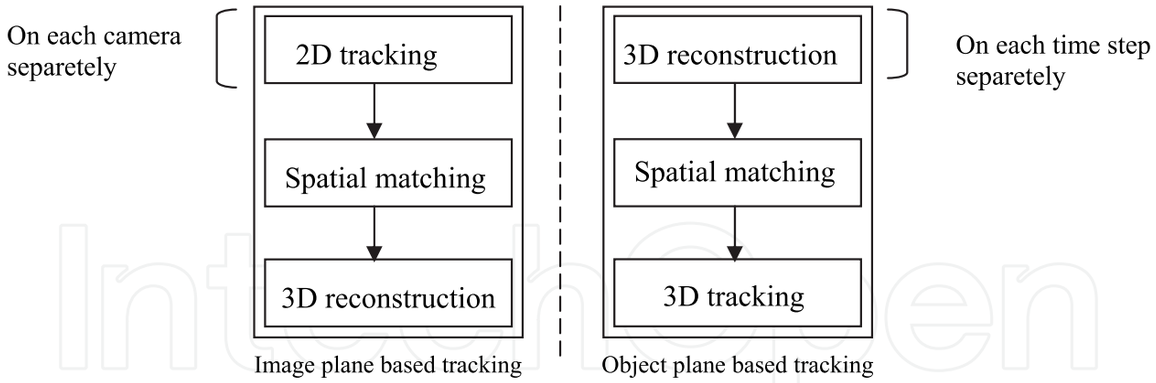

Fig. 11. Comparison of image and object plane based 3D tracking schemes.

function is applied in case any ambiguity arises. A detailed review of the particle tracking algorithms has been proposed by (Ouellette et al., 2006) and will not be repeated herein. The one proposed by (Biwole et al., 2009) is detailed here as an example:

3.3.1 2D tracking

Based on (Li et al., 2008) 2D tracking scheme, (Biwole et al., 2009) algorithm first utilizes a second order polynomial regression method to predict the center of the search region. The purpose of the regression is to minimize the changes in particle acceleration:

$$x_{\text{pixeli}} = \mathbf{a}t_i^2 + \mathrm{b}t_i + \mathrm{c} \tag{6}$$

where $\boldsymbol{x_{pixel}}$ stands for the pixel coordinates vector at instant time t and i stands for as much as 5 previous but not necessarily consecutive frames. Two by one constant vectors $\boldsymbol{a}$, $\boldsymbol{b}$ and $\boldsymbol{c}$ are acquired by least square fitting. Then, a cost function ϕ is used to resolve the conflicts within the search area:

$$\phi = \frac{\sqrt{\sum_{k=0}^{3}\left|\mathrm{D}_k - \mathrm{G}\tau_k - \mathrm{H}\right|^2}}{\sqrt{\sum_{k=0}^{3}\left|\mathrm{D}_k\right|^2}} \tag{7}$$

where $\boldsymbol{D_k}$ is the previously linked trajectory displacement between frames k and k+1, τ_k the middle time between frames k and $k+1$, and $\boldsymbol{G}$ and $\boldsymbol{H}$ the two by one constant vectors resulting from the linear regression of order 1 fitting $\boldsymbol{D_k}$ over frames 0 to 3:

$$\mathrm{D_k} \approx \mathrm{G}\tau_k + \mathrm{H} \tag{8}$$

The cost function thus appears as a regression residual normalized by a geometrical mean displacement. Its physical meaning is also to minimize the changes in particle acceleration. (Biwole et al., 2009) 2D tracking scheme includes four additional features. First, a "cross-gap" strategy accounts for particles undetected in a single frame. Whenever a particle is absent from the search region at frame n+1, the regression and the search is extended to frame n+2 based on the estimate and the trajectory goes on if a suitable particle is found. If a suitable particle is not found, the trajectory is ended. Second, particles centroids are recomputed at each frame (instead of doing it once and tracking them in 2D space). It allows starting new trajectories as new particles enter the field of vision. Third, an overlapping

trajectory detection step discards the shortest one of two trajectories with similar coordinates. This is done to compensate for the extra trajectories created by the previous step. Last, a bridging strategy connects parts of a same trajectory as follows: Let Te be a trajectory ending at frame t and Ts a trajectory starting at frame t or t+1. The cost function of a new trajectory composed of the last three positions of Te and the first three positions of Ts is calculated according to Equation 7. If the cost function is less than a preset parameter α (α is around 0.2), the bridge is validated.

This 2D tracking strategy is intended to yield longer trajectories than traditional ones. However, its computational cost in terms of space and time is higher than the cost generated by traditional algorithms. Going through the process with spatial matching at each time step would have been even more costly and error prone. This is why temporal tracking is done before spatial matching. As will be shown in section 5, 3D matching is later checked several times throughout the trajectory. A more detailed description of this 2D tracking scheme is given in (Li et al., 2008). The scheme was validated using simulated data of a jet flow impinging on a wall.

3.3.2 Stereo pair matching

Stereo pair matching also called spatial matching is first done using a three-camera arrangement. Firstly, the fundamental matrix of each pair of cameras is calculated. For two cameras 1 and 2, the fundamental matrix reads:

$$F_{12} = \left[T_1 - R_1 \cdot R_2^T \cdot T_2 \right]_\times R_1 \cdot R_2^T \tag{9}$$

Matrixes R_1, T_1, R_2 and T_2 are extrinsic parameters given by calibration. The cross-product [ ]x is defined as:

$$\left[u\right]_\times = \begin{pmatrix} 0 & -u_3 & u_2 \\ u_3 & 0 & -u_1 \\ -u_2 & u_1 & 0 \end{pmatrix} \tag{10}$$

Two 2D trajectories are considered matched if 6 pairs of time-synchronous points, one in each trajectory, can be found verifying the following equation:

$$\begin{bmatrix} x_1^t & y_1^t & 1 \end{bmatrix} F_{12} \begin{bmatrix} x_2^t \\ y_2^t \\ 1 \end{bmatrix} \prec s \tag{11}$$

where $\left(x_1^t, y_1^t\right)$ and $\left(x_2^t, y_2^t\right)$ are normalized pixel coordinates from each trajectory, t an instant time (t = 1..6), and s is a threshold value. Ideally, the left term of Equation (8) should equal zero but it never does, due to experimental and computational errors. This is why s is generally given the value 1. Tests showed that if Equation (11) is validated for at least 6 time-synchronous pairs of points, it is also validated for the others points of the two trajectories. Because of the possible high length of the trajectories, this strategy brings additional reliability in contrast to traditional 3D PTV algorithms where spatial matching is done only once before temporal tracking.

At first, each trajectory is matched using all three fundamental matrixes. The remaining unmatched trajectories are then matched using only one fundamental matrix. Those trajectories come from particles whose displacement is seen by only two cameras. After these two processes, the remaining unmatched trajectories are discarded.

3.3.3 3D reconstruction

This section deals with the calculation of final 3D coordinates from multiple views of a trajectory point. Let f = (f1,f2)T be the focal length in pixels, cc =(cc1,cc2)T the vector containing the principal point pixel coordinates, β the skew coefficient (scalar), k = (k1,k2,k3,k4,k5)T the vector containing the image radial (k1,k2,k3) and tangential (k4,k5) distortion coefficients given by calibration. Let P be a real world point of which the coordinates in the reference frame of one camera are (Xc,Yc,Zc). Let be xn = (x,y) the normalized projection of P on the camera image plane. Normalized coordinates are defined as the pinhole projection coordinates obtained when using a unit focal length (see Figure 3). We can write:

$$\mathrm{x_n} = \begin{bmatrix} x \\ y \end{bmatrix} = \begin{bmatrix} X_c / Z_c \\ Y_c / Z_c \end{bmatrix} \tag{12}$$

Taking into account the relation between each camera 3D reference frame XXc (Xc,Yc,Zc) and the calibration target 3D reference frame XX (X,Y,Z) given in Equation (4), Equation (12) can be rewritten for each camera i as:

$$\begin{cases} x_i = \dfrac{R_{11}^i X + R_{12}^i Y + R_{13}^i Z + T_1^i}{R_{31}^i X + R_{32}^i Y + R_{33}^i Z + T_3^i} \\ y_i = \dfrac{R_{21}^i X + R_{22}^i Y + R_{23}^i Z + T_2^i}{R_{31}^i X + R_{32}^i Y + R_{33}^i Z + T_3^i} \end{cases} \tag{13}$$

where by abuse of notation, T_i and R_i are the same as in Equation (4), and (x_i,y_i) are the normalized pixel coordinates of the particle on camera i. With i = [1...n] (n cameras), equation (10) gives rise to an overdeterminated system of 2n equations for only 3 unknowns which is solved by a least squares method. When the calibration target 3D reference frame is different from the final reference frame XXo = (Xo,Yo,Zo), equation (10) reads for each camera:

$$\begin{cases} \left[x\left(R_{31}U_{11} + R_{32}U_{21} + R_{33}U_{31}\right) - \left(R_{11}U_{11} + R_{12}U_{21} + R_{13}U_{31}\right)\right]X_0 + \\ \left[x\left(R_{31}U_{12} + R_{32}U_{22} + R_{33}U_{32}\right) - \left(R_{11}U_{12} + R_{12}U_{22} + R_{13}U_{32}\right)\right]Y_0 + \\ \left[x\left(R_{31}U_{13} + R_{32}U_{23} + R_{33}U_{33}\right) - \left(R_{11}U_{13} + R_{12}U_{23} + R_{13}U_{33}\right)\right]Z_0 \\ = -x\left(R_{31}V_1 + R_{32}V_2 + R_{33}V_3 + T_3\right) + \left(R_{11}V_1 + R_{12}V_2 + R_{13}V_3 + T_1\right) \\ \\ \left[y\left(R_{31}U_{11} + R_{32}U_{21} + R_{33}U_{31}\right) - \left(R_{21}U_{11} + R_{22}U_{21} + R_{23}U_{31}\right)\right]X_0 + \\ \left[y\left(R_{31}U_{12} + R_{32}U_{22} + R_{33}U_{32}\right) - \left(R_{21}U_{12} + R_{22}U_{22} + R_{23}U_{32}\right)\right]Y_0 + \\ \left[y\left(R_{31}U_{13} + R_{32}U_{23} + R_{33}U_{33}\right) - \left(R_{21}U_{13} + R_{22}U_{23} + R_{23}U_{33}\right)\right]Z_0 \\ = -y\left(R_{31}V_1 + R_{32}V_2 + R_{33}V_3 + T_3\right) + \left(R_{21}V_1 + R_{22}V_2 + R_{23}V_3 + T_2\right) \end{cases} \tag{14}$$

where U and V are respectively the matrices of rotation and translation to map from XX to XXo similarly to Equation (4). U and V are identical for all cameras and are calculated from the experimental set-up. Normalized pixel coordinates are related to actual pixel coordinates by the following rationale:
Let $r^2 = x^2+y^2$. After including lens distortion, the new normalized point coordinate xd is defined as follows:

$$\mathrm{x_d} = \begin{bmatrix} x_{d1} \\ x_{d2} \end{bmatrix} = (1 + k_1.r^2 + k_2.r^4 + k_5.r^6)\mathrm{x_n} + \mathrm{d_x} \tag{15}$$

where d_x is the tangential distortion vector (Heikkilä & Silvén, 1997 camera model):

$$\mathrm{d_x} = \begin{bmatrix} 2k_3.x.y + k_4.(r^2 + 2x^2) \\ \\ 2k_4.x.y + k_3.(r^2 + 2y^2) \end{bmatrix} \tag{16}$$

The final pixel coordinates $\mathrm{x_{pixel}}$ of the projection of P on the image plane reads:

$$\mathrm{x_{pixel}} = \begin{bmatrix} x_p \\ y_p \end{bmatrix} = \begin{bmatrix} f_1.(x_{d1} + \beta.x_{d2}) + cc_1 \\ f_2.x_{d2} + cc_2 \end{bmatrix} \tag{17}$$

Thus, from the knowledge of final pixel coordinates on at least 2 image planes, real 3D coordinates can be calculated.

4. Example of results

This section shows some examples of application of 3D PTV for indoor air flow measurement. Some helpful guidelines are given in terms of camera and light positioning, depending on the room layout and wall color. The following performance indicators will be used:

- "Tracking density" ratio ξ: it is the ratio of mean particle spacing (in a nearest neighbor sense) to mean particle displacement between two consecutive frames. It is an indicator of the tracking difficulty (Malik et al., 1993).
- "Correct tracking" ratio γ2D (respectively γ3D): Proposed by (Li 2008), it is the number of 2D (respectively 3D) tracked positions which are identical to the actual 2D/3D particle positions divided by the total number of tracked positions. This ratio only deals with tracked trajectories and is an indicator of the tracking accuracy. The actual 2D particle trajectories are estimated for each camera by adding up all the camera frames after background subtraction. The deviation from actual 3D positions is estimated by backprojection of calculated 3D trajectories on each camera image plane thanks to calibration data. A particle tracked position is considered "correct" when it is either identical to the actual particle position or its deviation from the latter position is less than the radius of the actual particle.
- "Total tracking" ratio $E_{3Dtrack}$ (respectively $E_{2Dtrack}$): proposed by (Malik et al., 1993) as the number of correctly tracked 3D (/2D) trajectories divided by the estimated total number of input 3D (/2D) trajectories.

4.1 3D PTV in a light-gray walled room, low density seeding

The test-room *MINIBAT* of the National Institute for Applied Sciences of Lyon, France, has two experimental cells of dimensions 3.1mx3.1mx2.5m high each (see Figure 12). The 3D PTV set-up included three cameras Dalsa 4M60 set at 1024x1024 pixels and 100 fps each. Each camera was mounted with a 15mm Canon lens with a 4.8 aperture. All cameras were placed in experimental room noted (6) on Figure 12. The recording computer was located in the other experimental room (7) and the door between the two rooms was closed to prevent heating up of the flow. Camera 3 was fixed onto the ceiling while cameras 1 and 2 were fixed on the walls as shown in Figure 13.

Light was provided by four 1000W compact fluorescent lamps situated in the climatic chamber (3) and separated from the airflow by the simple glass partition (4) to prevent heating up the flow. All lights were set at full power, with not shading grid. Walls of the test room are not black but light gray; consequently, it was found that better contrast between particles and background was achieved by directing the lights towards the walls and not directly towards the particles; therefore, helium filled soap bubbles were indirectly illuminated by reflection of the light from walls and ceiling. The calibration target consisted of a planar checkerboard composed of black and white 30mm-large squares. The checkerboard had 12 horizontal squares and 8 vertical squares as shown in Figure 14. The calibration algorithm by (Bouguet, 2002) was used. Bubbles were released upward. Index ξ equaled 3.9, 8.1 and 6.3 respectively for cameras 1, 2 and 3, which corresponds to a low density seeding.

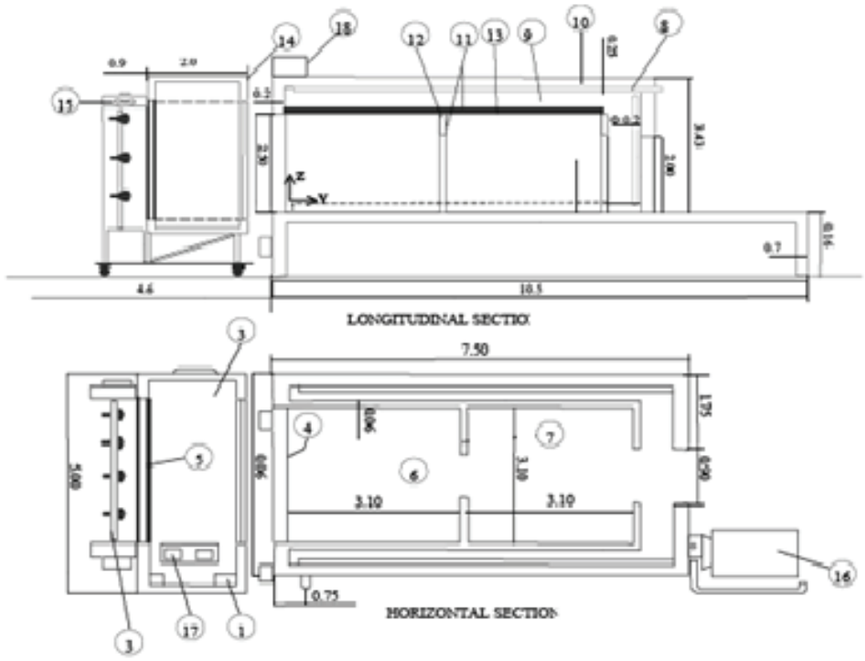

(1) cold conditioner; (2) spotlights; (3) climatic chamber;
(4) simple glass; (5) double glass; (6) experimental room; (7) experimental room;
(8) air pipe; (9) thermal guard; (10) insulated concrete;
(11) plaster plate ; (12) wood plate; (13) wood plate;

Fig. 12. Mock-up of the test-room MINIBAT. Lights were situated behind the glass (4) in the climatic chamber (3), cameras were situated in the experimental room (6) and the recording computer in experimental room (7)

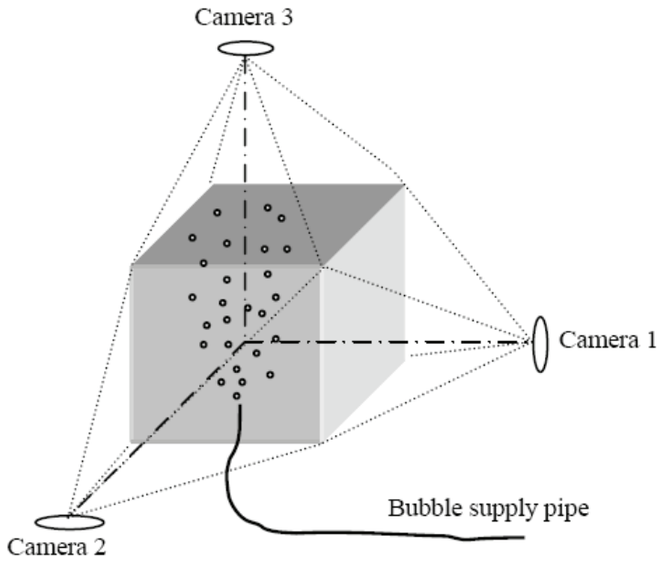

Fig. 13. Camera positioning for 3D PTV on an ascendant free flow.

Fig. 14. Calibration target as observed from camera 2 viewpoint.

Full 3D displacement of particles over 10 frames is shown in Figure 15. The average $E_{2Dtrack}$ was 82% over the three cameras with $\gamma_{2D} = 1$. We found $E_{3Dtrack}$= 88% with $\gamma_{3D} = 0.9$. Having $E_{3Dtrack} > E_{2Dtrack}$ is readily explainable by the fact that some extra 3D trajectories were produced from particles seen by only two cameras at a time. It is also normal to have $\gamma_{3D} < \gamma_{2D}$ because of additional errors due to computational approximations when calculating the 3D coordinates.

For validation purpose, all 3D trajectories were projected back onto each camera image plane and compared with the real 2D bubbles trajectories obtained by adding up the original images. The resulting images for cameras 1 and 2 are shown on Figure 16. On the Figure, untracked white streaks are trajectories from particles seen by only one camera.

From 3D data, the calculated bubbles mean velocity was 0.375m/s with a minimum at 0.206m/s for bubbles far from the pipe nozzle, and a maximum at 0.651m/s.

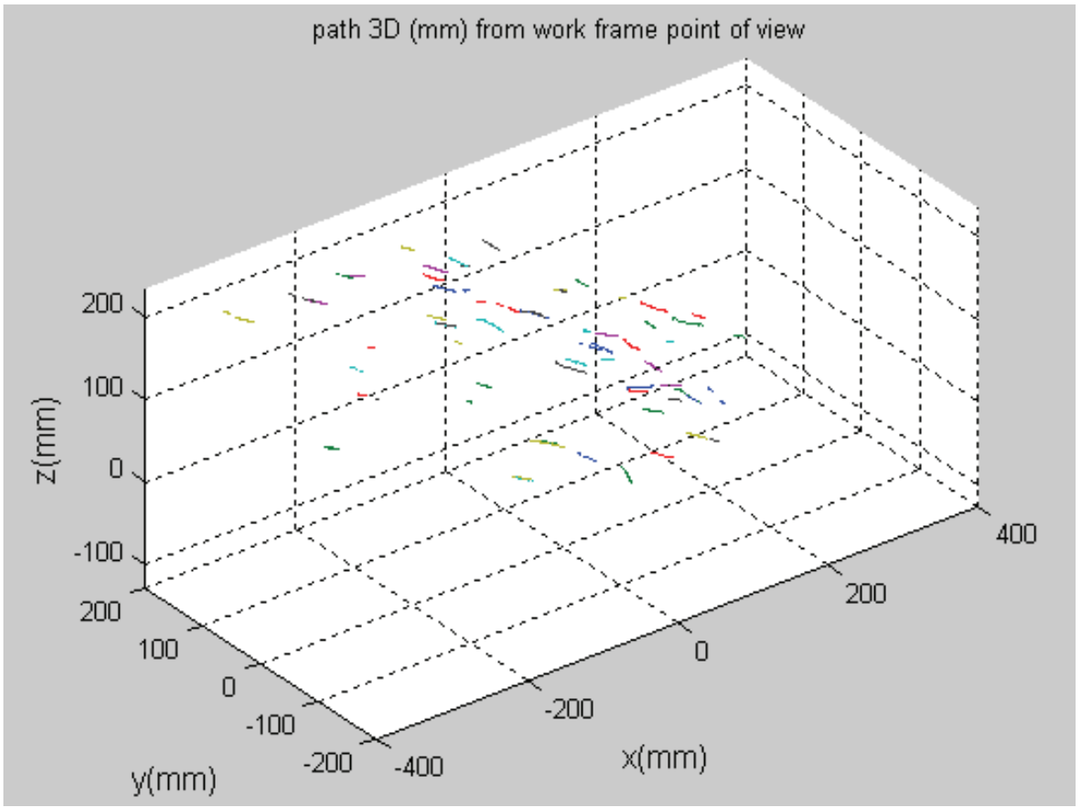

Fig. 15. 3D path (mm) of tracked particles. The orientation of axes is given by the calibration target.

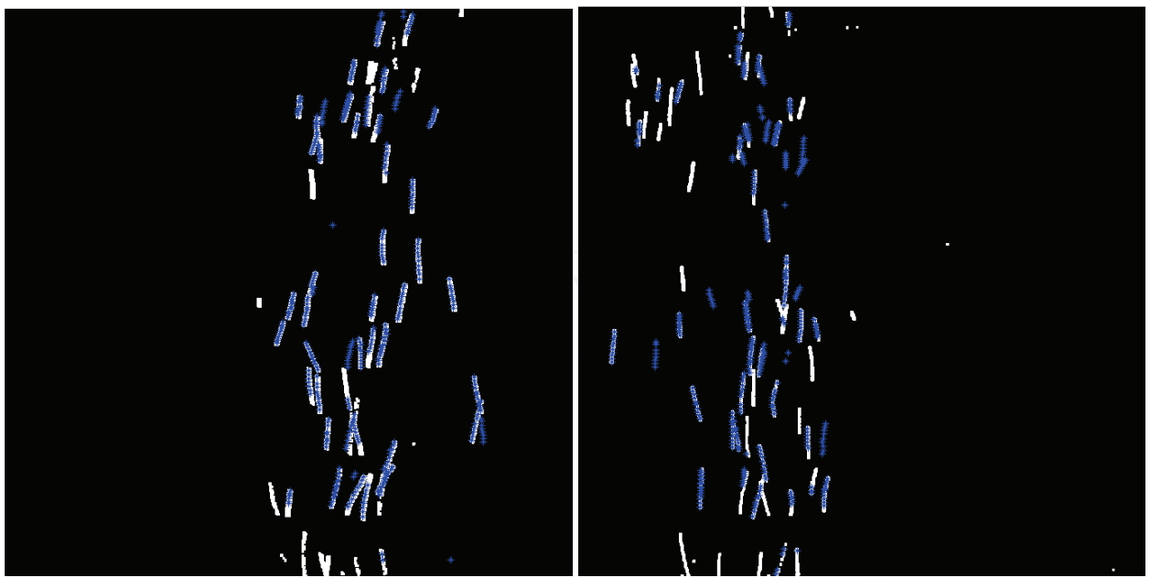

(a) (b)

Fig. 16. Comparison of real trajectories (white) versus backprojected 3D trajectories (blue) on cameras 1 (Figure 16a) and 2 (Figure 16b). Completely white tracks are particle trajectories that are seen by only one camera and therefore are not traceable in 3D space.

4.2 3D PTV in a black-walled room, high density seeding

Helium filled soap bubbles were released in the 5.5mx3.7x2.4m high *Room Ventilation Simulator* at the Bio Environmental Engineering laboratory, University of Illinois at Urbana-Champaign, USA. The bubbles were released from two converging pipes and the production was stopped 10s before the recording. To increase the measurement area, camera 3 was not situated directly above the measurement volume but at an angle of 45° as shown in Figure 17. The planar angle between each camera was approximately 120° with six 500W spotlights situated onto the horizontal bisectors. To prevent heating, the spotlights were turned on only for the two seconds of recording. Cameras were set at 30 fps. Calibration was done using the same calibration target as described above.

Index ξ equalled 3.3, 2.2, and 2.5 respectively for cameras 1, 2 and 3. Such values for ξ correspond to a difficult particle tracking situation (see Figure 18). The temporal tracking process yielded $E_{2Dtrack}$ = 670/1566 for camera 1, 314/889 for camera 2 and 581/1635 for camera 3 with an average γ_{2D} = 0.9. We found $E_{3Dtrack} \approx$ 714/1800 with γ_{3D} = 0.75. Whereas the common view area was only 1.5mx1.5mx1m, the actual measured area was approximately 3mx3mx1.2m as shown on Figure 19. This is due to the fact that 3D coordinates are still calculated if the particles are seen by only two cameras. Figure 19 also shows the individual path of a bubble and validation by back-projection is shown in Figure 10-11. From the 3D data, the calculated bubbles mean velocity was found equal to 0.107m/s with a minimum at 0.015m/s and a maximum at 0.521m/s.

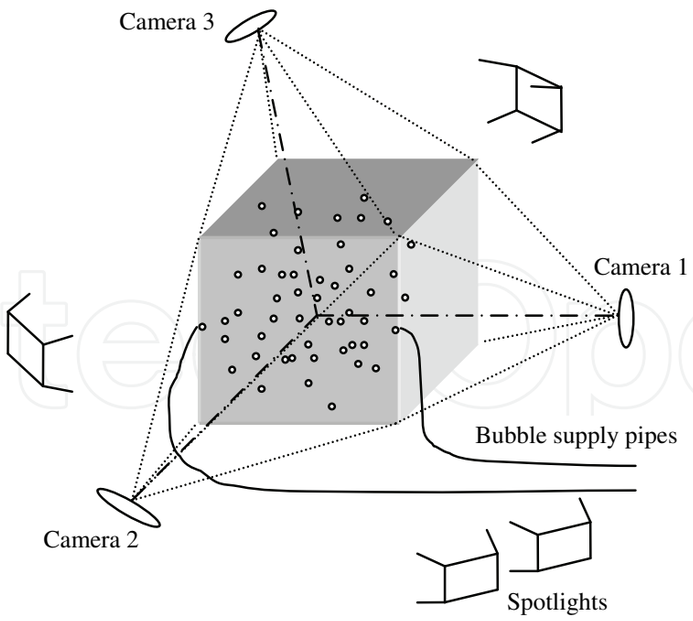

Fig. 17. Camera and light positioning for 3D PTV in a black-walled room.

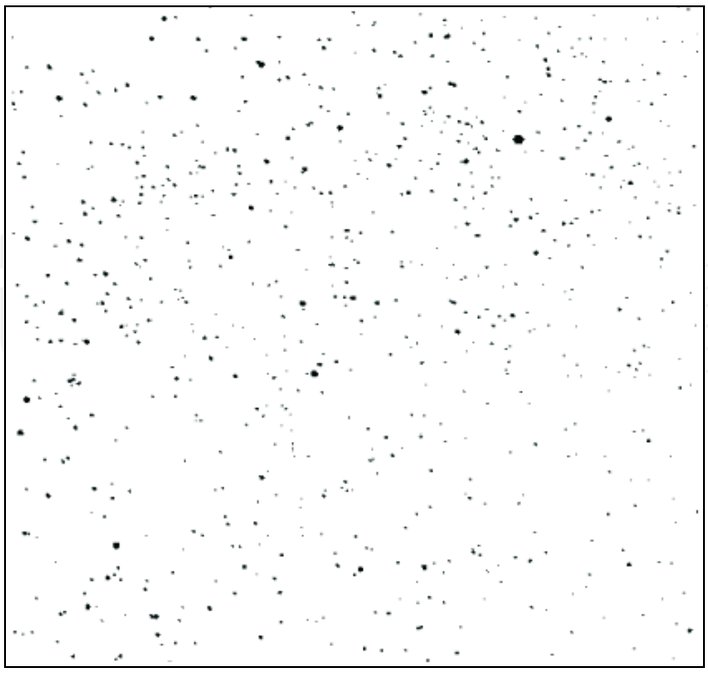

Fig. 18. Particle images from a region of camera 1 after image processing (inverted and 100% zoomed in image).

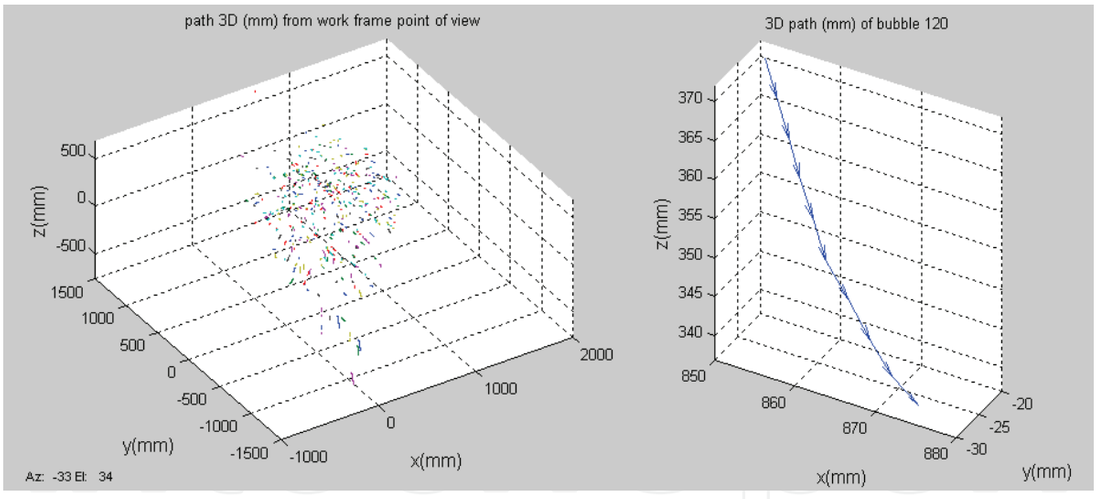

Fig. 19. 3D path of bubbles over 40 frames in high density case and 3D path of a single bubble over 10 frames.

4.3 Velocity distribution over a heat source

An electric heater was placed against one wall of the *Room Ventilation Simulator*. Helium filled bubbles were emitted from two pipes situated on both sides of the radiator. The bubble generation was not stopped during the recording to prevent their rarefaction due to the upward convection flow. In order to avoid any impact of the bubble initial velocity (5.33m/s) on the measured flow, the pipes nozzles were facing downwards. Therefore, the tracers were recorded from the radiator height of 90cm after rebounding on the floor.

One camera was placed parallel to the wall and looking downward at the field. The other two were facing the wall at a symmetrical angle of 45° as shown on Figure 20. To avoid illuminating the background (wall), the spotlights were also placed parallel to the wall on both sides of the heater. The targeted measurement field was the area above the heater. Therefore, the calibration target was placed over the heater as shown in Figure 21. The heating power was set at 600W. Eight T type thermocouples were set to record the temperature of the wall and of the air above the heater at 10cm from the wall. The temperature distribution was 28.5°C on the wall, 29.8°C above the heater and 29.2°C at the center of the room six feet from the wall and three feet from the floor.
Due to the chimney effect, many particles were driven out of the measurement field. Therefore, the tracking was performed in low density. Index ξ was 3.3, 3.9, and 4.8 respectively for cameras 1, 2 and 3. Results of 3D PTV over the heater are shown in figures 22 and 23. The measured area was approximately 1.5m x 0.9m x 1.5m high. Temporal tracking yielded E2Dtrack = 95/138 for camera 1, 73/90 for camera 2 and 61/65 for camera 3 with γ2D = 1. We found E3Dtrack ≈ 106/140 with γ3D = 0.95. The maximum velocity was 0.851m/s for a bubble situated above the heater.

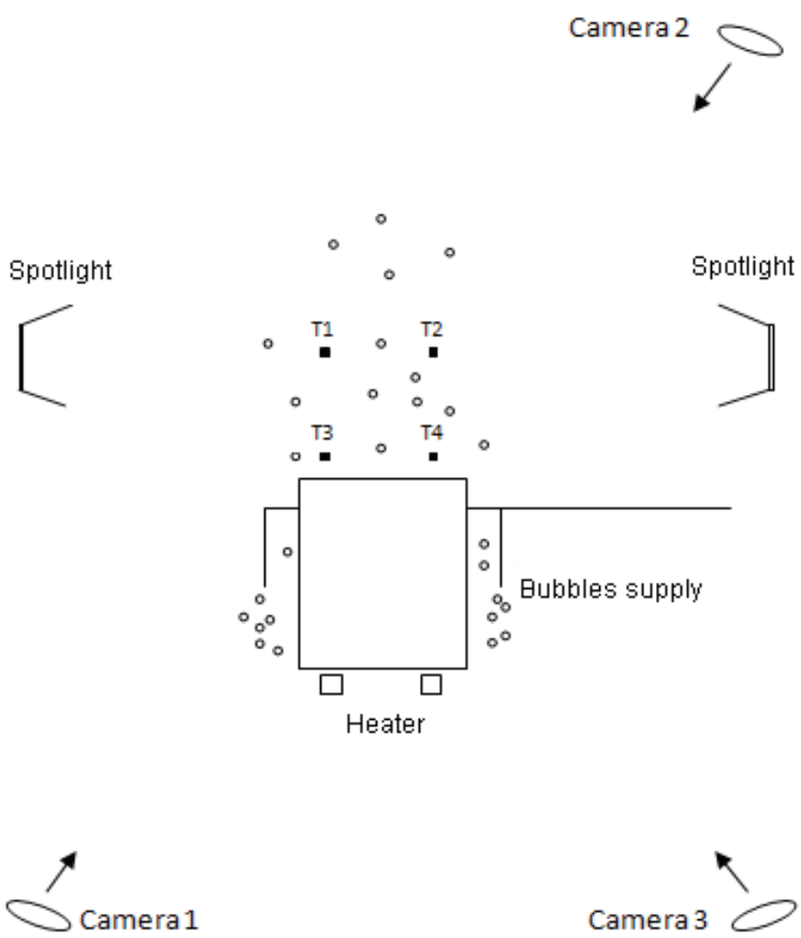

Fig. 20. Cameras and light sources positioned for 3D PTV over a heater

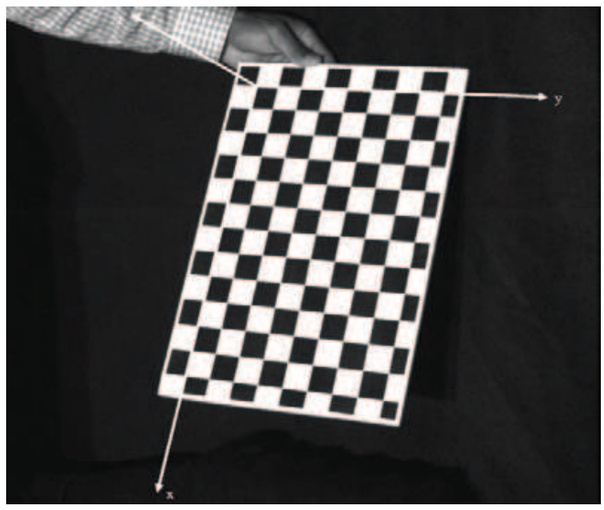

Fig. 21. Calibration target reference frame from camera 3 viewpoint

(a) (b)

(c)

Fig. 22. White arrows show the bubbles 3D trajectories projected on image plane of cameras 1, 2 and 3 (respectively figures 17a, 17b and 17c). The measured area is approximately 1.5m x 0.9m x 1.5m high.

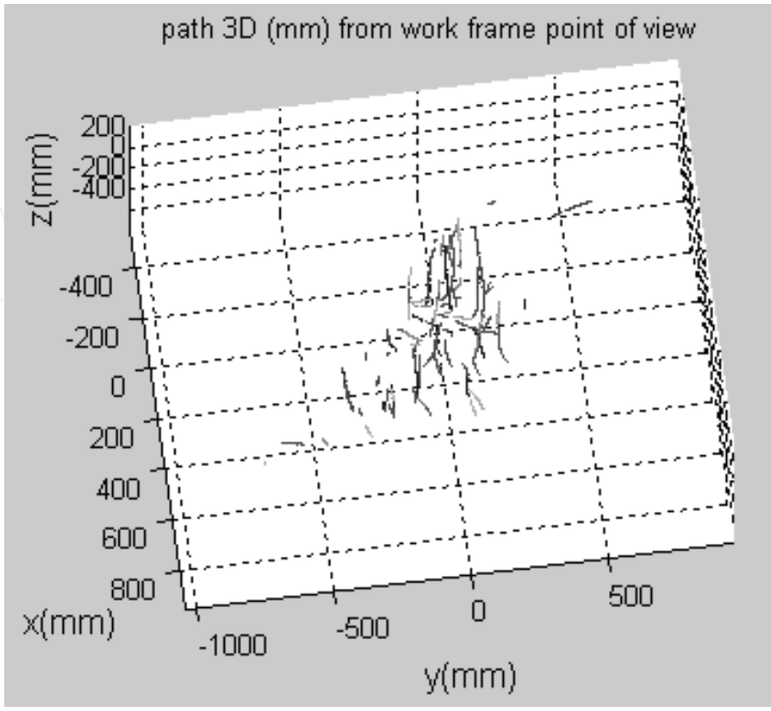

Fig. 23. 3D path of bubbles above the heater throughout 30 frames

4.4 Velocity distribution in an experimental aircraft cabin

The experimental aircraft cabin used is part of the Bio-Environmental Engineering laboratory test facilities. It is a full-scale, fully equipped five row section of a Boeing 767-300 with dummies to simulate passengers as shown in Figure 24. The cabin is 4m x 3m x 2m high. Helium filled bubbles were introduced from two pipes situated at the sides of the ceiling middle section. The aircraft ventilation system was on. Three cameras were placed outside of the cabin in a triangular pattern. They were directed convergently, with a large triangle base. The calibration target was a planar checkerboard composed of a 12 x 12 array of 6cm black and white squares as shown in Figure 25. Light was provided by eight 120W light bulbs. Two extra 500W spots were facing the cabin from the external side of the glass wall.

After bubble seeding, index ξ was 2.1, 2.3, and 2.3 respectively for cameras 1, 2 and 3. After temporal tracking, $E_{2Dtrack}$ averaged 0.4 over the three cameras with $\gamma_{2D} = 1$. Full 3D tracking yielded $E_{3Dtrack} = 0.63$ with $\gamma_{3D} = 0.7$. A total of 1083 particles were 3D tracked. Velocity profiles obtained (see Figure 26) were found similar to those obtained by (Wang et al., 2005) on the same experimental set-up. Especially, the same vortices due to recirculation of the air over the two aisles could be observed and 3D tracked. The mean velocity equaled 0.48m/s over the cabin, with a minimum at 0.018m/s which means quasi static air far from the ventilation nozzles. The 3D data enabled the tracking of the air trajectory and the precise identification of areas of minimum air displacement.

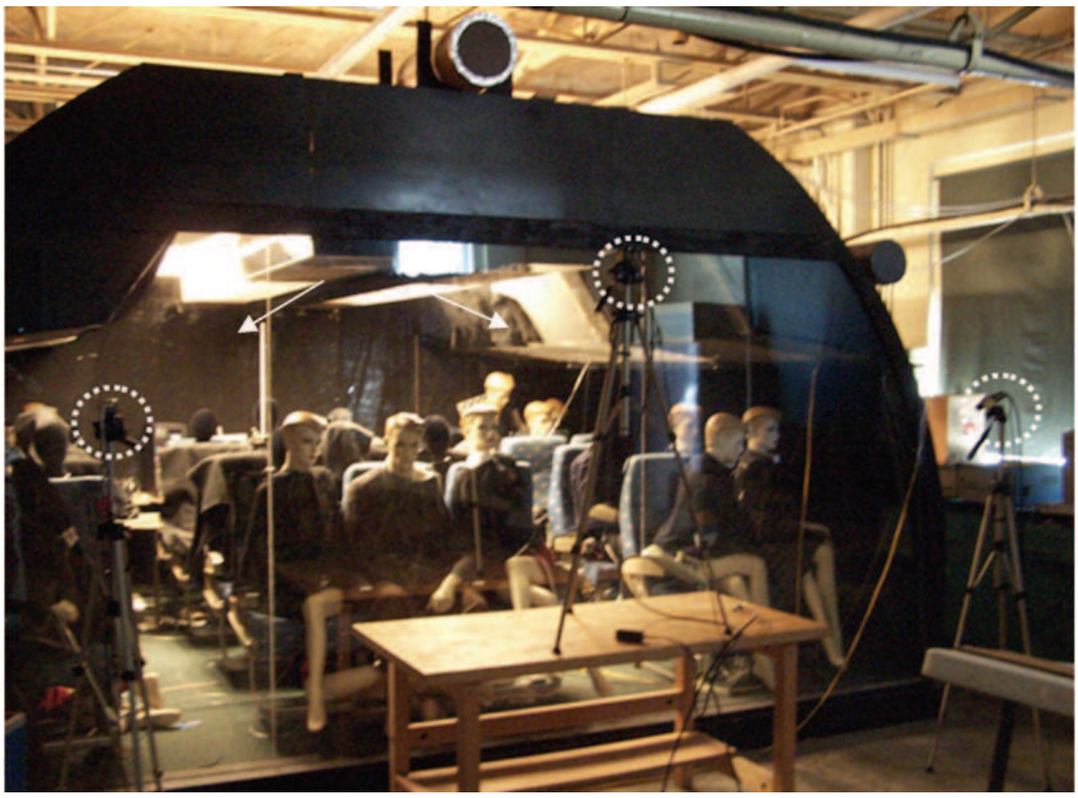

Fig. 24. Experimental aircraft cabin. Cameras positions are marked by white circles. The two ventilation inlets are marked by white arrows.

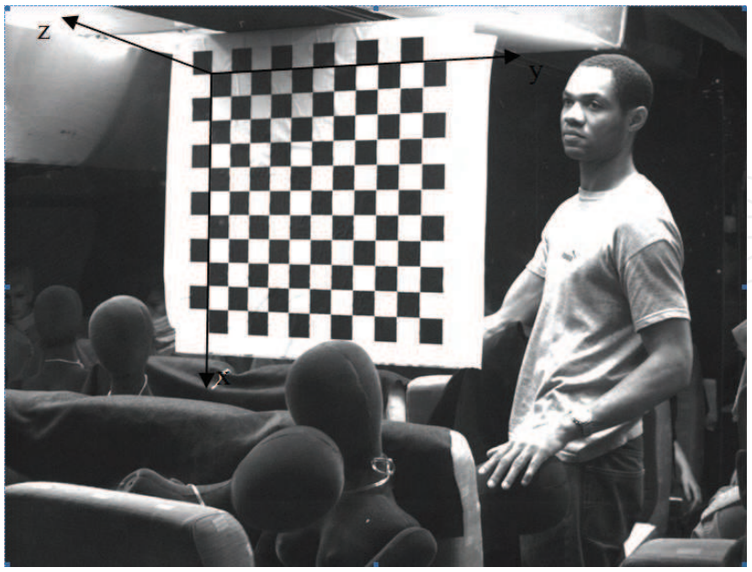

Fig. 25. Calibration target reference frame from camera 1 viewpoint

Fig. 26. Instantaneous 2D velocity in the aircraft cabin using the fast normalized cross-correlation temporal tracking scheme. Vortices due to recirculation of the air in the cabin can be seen over the aisles. University of Illinois at Urbana-Champaign, Department of Agricultural and Biological Engineering, Bioengineering Research Laboratory, USA

5. Conclusion and prospective research

Recent developments in large scale three dimensional particle tracking velocimetry have proven that this technique is suitable for the quantitative measurement en indoor airflow and pollutant dispersion. The technological breakthrough comes first from two aspects: first the measurement of the air velocity is no longer point-wise like in hot wire anemometry, or planar like in stereoscopic particle image velocimetry. On the contrary, the measurement is volumetric, with the 3D velocity of several points acquired simultaneously in large volumes. Second precise air and pollutants trajectories are acquired versus time. This chapter has presented typical experimental set-ups and algorithms that could be used to that purpose. The algorithm by (Biwole et al., 2009) has been detailed as an example. Around 1400 neutrally buoyant particles made of helium filled bubbles were tracked in volumes up to $3m^3$. The illumination was provided by halogen lamps. It was also shown that lighting up the helium filled bubbles by indirect reflection of the light on walls and ceiling allows a better particle detection on non black-walled rooms.

Current research on the subject aims at several objectives. Firstly, scientists try to increase the seeding density which is still limited to less than 2000 particle because of occlusion problems. A densely seeded volume would allow a finer understanding of the flow topology and a better modeling by CFD simulation. The measured indoor volumes can also be extended by juxtaposing several multi-camera 3D PTV arrangements. Secondly, researchers try to increase the range of measurable speeds by the design of algorithms coupling large scale 3D PTV with large scale three dimensional particle streak velocimetry. The latter technique comes in to capture the velocity of particles which cannot be detected as dots by the cameras because of their higher speed. In rooms, such speeds can be found at air inlets and outlets. Thirdly, researchers try to combining particles Lagrangian velocity with particles Lagrangian temperature. Trying to do so by monitoring the expansion of bubbles volume due to temperature is nearly impossible because of the low coefficient of volumetric thermal expansion of helium. The most realistic approach is to look for fluorescent bubble shells that visually and reversibly change colors at predetermined temperatures. In this regard, the use of thermochromic liquid crystals or of polythiophene films could be of some help.

6. References

Adamczyk, A.A. & Rimai, L. (1988). Reconstruction of a 3-dimensional flow field from orthogonal views of seed track video images. *Experiments in Fluids,* Vol.6, No.6, pp. 380-386

Adrian, R.J. (1991). Particle-imaging techniques for experimental fluid mechanics. Annual Review of Fluid Mechanics, Vol.23, pp. 261–304

Biwole, P.H.; Krauss G.; Favier, E; Rusaouen, G. & Roux J.-J. (2008). Non-stereoscopic 3D particle tracking velocimetry for full scale rooms, *Proceedings of Advanced building ventilation and environmental technology for addressing climate change issues*, Kyoto, Japan, October 2008

Biwole, P.H.; Yan, W.; Zhang, Y. & Roux, J-J. (2009). A complete 3D particle tracking algorithm and its applications to indoor airflow study. *Measurement Science and Technology*, Vol.20, 115403 (13 pp)

Bougnoux, S. (1998). From projective to Euclidean space under practical situation, a criticism of self calibration, *Proceedings of the 6th European conference on computer vision*, pp. 790-796, January 1998

Bouguet, J-Y. (2002). *Camera Calibration Toolbox for Matlab*, Available from http://www.vision.caltech.edu/bouguetj/calib_doc/

Caprile, B. & Torre, V. (1990). Using vanishing points for camera calibration. *The International Journal of Computer Vision* Vol.4, No.2, pp. 127-140

Carosone, F.; Cenedese, A. & Querzoli, G. (1995). Recognition of partially overlapped particle images using the Kohonen neural network. *Experiments in Fluids*, Vol.19, pp. 225–232

Crouser, P.D.; Bethea, M.D. & Merat, F.L. (1997). Unattenuated tracer particle extraction through time-averaged, background image subtraction with outlier rejection. *Experiments in Fluids*, Vol.22, No.3, pp. 220-228

Dimotakis, P.E.; Debussy, F.D. & Koochesfahani, M.M. (1981). Particle streak velocity field in two-dimensional mixing layer. *Physics of Fluids*, Vol.24, p. 995

Engelmann, D.; Garbe, C.; Stšhr, M.; Geissler, P.; Hering, F. & Jähne, B. (1998). Stereo Particle Tracking, *Proceedings of the 8th International Symposium on Flow Visualisation*, pages 240.1249.9, Sorrento, Italy, September 1-4, 1998

Engelmann, D. (2000). *3D-Flow Measurement by Stereo Imaging*, Dissertation, Rupertus Carola University of Heidelberg, Germany.

Faugeras, O. (1993). *Three-dimensionl computer vision: a geometric viewpoint*, MIT press, London, 1993, 663 p.

Fanger, P.O. (1970). *Thermal comfort: analysis and applications in environmental engineering,* Mc Graw Hill ed., New-York, 1970, 244p.

Ge, Y. & Cha, S.S. (2000). Application of Neural Networks to Spectoscopic Imaging Velocimetry. *AIAA Journal*, Vol.38, pp 487-492

Gruen, A. & Baltsavias, E. (1988). Geometrically constrained multi-photo matching. *Photogrammetric Engineering,* Vol.54, pp. 633-641

Guezennec, Y.G.; Brodkey, R.S.; Trigui, N. & Kent J.C. (1994). Algorithms for fully automated three-dimensional particle tracking velocimetry. *Experiments in Fluids*, Vol.17, pp. 209–219

Hartley, R. (1994). Self calibration from multiple views with a rotating camera, *Proceedings of 3rd European Conference on Computer Vision*, pp. 471-478, Stockholm, Sweden, May, 1994

Heikkilä J. & Silvén O. (1997). A Four step camera calibration procedure with implicit image correction, *Conference on Computer Vision and Pattern Recognition (CVPR'97)*, San Juan, Puerto Rico, 1997

Hough P. (1962). *Method and means for recognizing complex patterns*, U.S. Patent 3069654

Jähne, B. (1997). *Digitale Bildverarbeitung. 4. Außage*, Springer Verlag

Kasagi, N. & Sata, Y. (1992). Recent developments in three-dimensional particle tracking velocimetry. *Proceedings of the 6th International Symposium on Flow Visualization*, pp. 832-837, Yokohama, Japan, October, 1992

Kessler, M. & Leith, D. (1991). Flow measurement and efficiency modeling of cyclones for particle collection, *Aerosol Science and Technology* 15, pp. 8-18

Kerho, M.F. & Bragg M.B. (1994). Neutrally buoyant bubbles used as flow tracers in air, *Experiments in Fluids* 6, pp. 393-400

Lee, S.J. & Kim, S. (2005). Simultaneous measurement of size and velocity of microbubbles in opaque tube using
X-ray particle tracking velocimetry technique. *Experiments in Fluids*, Vol.39, No.3, pp. 492-497

Li, D.; Zhang, Y.; Sun, Y. & Yan W. (2008). A multi-frame particle tracking algorithm robust against input noise, *Measurement Science and Technology* 19, 105401 (11pp)

Liebowitz, D. & Zisserman, A. (1998). Metric rectification for perspective images of planes. *Proceedings of IEEE conference on computer vision and pattern recognition, Santa Barbara, California, June 1998,* pp. 482-488

Luong, Q.T. & Faugeras, O. (1997). Self-calibration of a moving camera from point correspondences and fundamental matrices, *The International Journal of Computer Vision* 22 (3), pp. 261-289

Maas, H.G. (1992) Complexity analysis for the establishment of image correspondences of dense spatial target fields, *International Advances of Photogrammetry and Remote Sensing*, XXIX (B5), pp. 102-107

Maas, H.G.; Gruen, A. & Papantonious, D. (1993). Particle tracking velocimetry in three-dimensional flows, Experiments *in Fluids* 15, pp. 133-146

Machacek, M. (2002). A Quantitative Visualization Tool for Large Wind Tunnel Experiments. PhD Thesis, Zurich: Swiss Federal Institute of Technology

Malik, N.A.; Dracos, Th. & Papantoniou, D.A. (1993). Particle tracking velocimetry in three-dimensional flows—part 2: Particle tracking. *Experiments in Fluids* 15, pp. 279–294

Mann J., Ott S. & Andersen J.S. (1999). *Experimental study of relative, turbulent diffusion*, Risø National Laboratory Report Risø-R-1036 (EN)

Maxey, M.R. & Riley, J.J. (1983). Equation of motion of a small rigid sphere in a nonuniform flow. *Physics of Fluids* Vol.26, No.4, pp. 883-889

Maybank, S.J. & Faugeras, O. (1992). A theory of self-calibration of a moving camera. *The International Journal of Computer Vision,* Vol.8, No.2, pp. 123-152

Melling, A. (1997). Tracer particles and seeding for particle image velocimetry. *Measurement Science and Technology,* Vol.8, pp. 1406-1416

Muller, D. & Renz, U. (1996). Determination of all airflow velocity components by a particle-image-velocimetry system, *Proceedings of 5th International Conference on Air Distribution in Rooms: ROOMVENT'96*, pp. 413-419, Yokohama, Japan, July 17-19, 1996

Nishino, K.; Kasagi, N. & Hirata, M. (1989). Three-dimensional Particle Tracking Velocimetry based on automated digital image processing. *Journal of Fluid Engineering*, Vol.111, pp. 384-391

Nishino, K. & Kasagi, N. (1989). Turbulence statistics in a two-dimensional channel ßow using a three-dimensional Particle Tracking Velocimeter, Proceedings on the Seventh Symposium on Turbulent Sheer Flows, Stanford University, August 21-23

Nobach, H. & Honkanen, M. (2005). Two-dimensional Gaussian regression for sub-pixel displacement estimation in particle image velocimetry or particle position estimation in particle tracking velocimetry. *Experiments in Fluids*, Vol.38, No.4, pp. 511-515

Okuno, Y.; Fukuda, T.; Miwata, Y. & Kobayashi, T. (1993). Development of three-dimensional air flow measuring method using soap bubbles. *Japanese Society of Automotive Engineers (JSAE) Review,* Vol.14, No.4, pp. 50-55

Otsu, N. (1979). A threshold selection method from gray-level histogram. *IEEE Transactions on Systems, Man, and Cybernetics*, Vol.9, No.1, pp. 62-66

Ouellette, N.T.; Xu, H. & Bodenschatz, E. (2006). A quantitative study of three-dimensional Lagrangian particle tracking algorithms. *Experiments in Fluids,* Vol.40, pp. 301–313

Papantoniou, D. & Dracos, T. (1989). Analyzing 3-Dimensional Turbulent Motions in Open Channel Flow by Use of Stereoscopy and Particle Tracking, In: *Advances in Turbulence 2,* Hernholz & Fiedler, Springer Verlag, Heidelberg

Sata, Y.; Sato, K.; Kasagi, N. & Takamura, N. (1994). Application of the three-dimensional particle tracking velocimeter to a turbulent air flow, In: *Proceedings of the 3rd Asian Symposium on Visualization*, Y., Nakayama, Springer-Verlag, pp. 705-709

Scholzen, F. & Moser, A. (1996). Three-dimensional particle streak velocimetry for room air flows with automatic stereo-photogrammetric image processing, *Proceedings of 5th International Conference on Air Distribution in Rooms: ROOMVENT'96*, pp. 555-562, Yokohama, Japan, July 17-19, 1996

Stein, G. (1995). Accurate internal camera calibration using rotation, with analysis of sources of errors. *Proceedings of the 5th International Conference on Computer Vision,* pp. 230-236, Cambridge, Massachusetts, June 1995

Sun, Y. & Zhang, Y. (2003). Development of a stereoscopic particle image velocimetry system for full-scale room airflow studies, Part II: experimental setup. *Transaction of the American society of Heating, Refrigerating and Air-Conditioning Engineers (ASHRAE)*, Vol.9, No.2, pp. 540-548

Suzuki, Y. & Kasagi, N. (1999). Turbulent air-flow measurement with the aid of 3-D particle tracking velocimetry in a curved square bend. *Flow, Turbulence and Combustion,* Vol. 3, pp. 415-442

Suzuki, Y.; Ikenoya, M. & Kasagi, N. (2000) Simultaneous measurement of fluid and dispersed phases in a particle-laden turbulent channel flow with the aid of 3-D PTV. *Experiments in Fluids*, Vol.29, pp. 185-193

Teh, Ch. & Chin, R. (1988). On image analysis by the method of moments. *IEEE Pattern Analysis and Machine Intelligence,* Vol.10, No.6, pp. 496-513

Wang, A.; Zhang, Y.; Sun, Y. & Wang, X. (2005). Experimental study of ventilation effectiveness and air velocity distribution in an aircraft cabin mock up. *Building and Environment*, Vol. 43, n° 3, pp. 337-343

Wierzimok, D. & Hering, F. (1993). Quantitative Imaging of Transport in Fluids with Digital Image Processing, In *Imaging in Transport Processes*, Begell House, pp 297-308

Willneff, J. & Gruen, A. (2002). A new spatio-temporal matching algorithm for 3D-ParticleTracking Velocimetry, *Proceeding of The 9th International Symposium on Transport Phenomena and Dynamics of Rotating Machinery,* Honolulu, Hawaii, USA, Feb 10-14, 2002

Virant, M. (1996). *Anwendung der dreidimensionalen "Particle Tracking Velocimetry" auf die Untersuchung von Dispersionsvorgšngen in Kanalstršmungen*, ETH Zürich - Dissertation Nr. 11678

Virant, M & Dracos, T. (1997). 3D PTV and its application on Lagrangian motion. *Measurement Science and Technology,* Vol. 8, 1539-52

Zhao, L.; Zhang, Y.; Wang, X.; Riskowski, G.L. & Christianson, L.L. (1999). Measurement of airflow pattern in ventilated spaces using particle image velocimetry, *Proceedings of ASAE/CSAE Annual International Meeting,* paper #994156, Toronto, Ontario, Canada, 1999

Zhang, Zhengyou. (1999). Flexible camera calibration by viewing a plane from unknown orientations, *Proceedings of the International Conference on Computer Vision (ICCV'99),* pp. 666-673, IEEE 0-7695-0164-8/99, Kerkyra, Greece, September 20-27, 1999

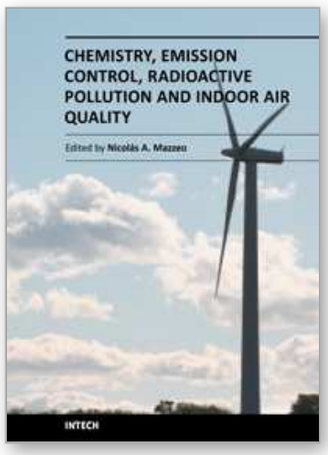

Chemistry, Emission Control, Radioactive Pollution and Indoor Air Quality

Edited by Dr. Nicolas Mazzeo

ISBN 978-953-307-316-3
Hard cover, 680 pages
Publisher InTech
Published online 27, July, 2011
Published in print edition July, 2011

The atmosphere may be our most precious resource. Accordingly, the balance between its use and protection is a high priority for our civilization. While many of us would consider air pollution to be an issue that the modern world has resolved to a greater extent, it still appears to have considerable influence on the global environment. In many countries with ambitious economic growth targets the acceptable levels of air pollution have been transgressed. Serious respiratory disease related problems have been identified with both indoor and outdoor pollution throughout the world. The 25 chapters of this book deal with several air pollution issues grouped into the following sections: a) air pollution chemistry; b) air pollutant emission control; c) radioactive pollution and d) indoor air quality.

InTech Europe
University Campus STeP Ri
Slavka Krautzeka 83/A
51000 Rijeka, Croatia
Phone: +385 (51) 770 447
Fax: +385 (51) 686 166
www.intechopen.com

InTech China
Unit 405, Office Block, Hotel Equatorial Shanghai
No.65, Yan An Road (West), Shanghai, 200040, China
中国上海市延安西路65号上海国际贵都大饭店办公楼405单元
Phone: +86-21-62489820
Fax: +86-21-62489821

IntechOpen